



Variational Monte Carlo study of symmetric mass generation in a bilayer honeycomb lattice model

 Wanda Hou and Yi-Zhuang You 

Department of Physics, University of California at San Diego, La Jolla, California 92093, USA

 (Received 5 January 2023; revised 28 August 2023; accepted 29 August 2023; published 20 September 2023)

We investigate a bilayer honeycomb lattice model of spin-1/2 fermions at half-filling with local Heisenberg coupling of fermion spins across the two layers. Using variational Monte Carlo (VMC) simulation, we demonstrate that the system undergoes a direct transition from a Dirac semimetal phase to a symmetric gapped phase, known as symmetric mass generation (SMG), as the Heisenberg coupling strength is increased. The transition does not involve spontaneous symmetry breaking or topological order and has been proposed as an example of the fermionic deconfined quantum critical point (fDQCP). Our simulation shows that a fermionic parton bilinear mass opens at the transition point while all symmetries are still preserved thanks to the quantum fluctuations introduced by the correlation factor in the variational wave function. From the simulation data, we extract the critical exponent $\nu = 0.96 \pm 0.03$ and the fermion scaling dimension $\Delta_c = 1.31 \pm 0.04$ at the SMG critical point, which are consistent with the field theoretical prediction of fDQCP in (2+1)D. These findings support the hypothesis that the fermion fractionalizes at the SMG critical point.

 DOI: [10.1103/PhysRevB.108.125130](https://doi.org/10.1103/PhysRevB.108.125130)

I. INTRODUCTION

Symmetric mass generation (SMG) [1] is a mechanism by which gapless Dirac fermions acquire a gap in their excitation spectrum without breaking symmetry or developing topological order. The gap-opening transition, known as the SMG transition, involves nonperturbative interaction effects among the fermions and does not require any fermion bilinear mass condensation, in contrast to the conventional Higgs mechanism [2–6]. Numerical simulations [7–17] have shown that the SMG transition can be a direct and continuous quantum critical point in various models, which is intriguing because it does not fit the Landau-Ginzburg-Wilson paradigm, as the phases on either side are not distinguished by any symmetry-breaking order parameter. It has been suggested [18,19] that the SMG critical point is described by a *fermionic* version of the deconfined quantum critical point (DQCP) [20–23], in which fermions *fractionalize* into deconfined bosonic and fermionic partons at (and only at) the critical point. However, numerical evidence for the fermion fractionalization is still lacking.

The goal of this study is to understand the universal properties of the SMG transition and provide evidence for the fermion fractionalization hypothesis. To this end, we examine a bilayer honeycomb lattice model of interacting fermions and investigate the SMG transition using numerical and analytical methods. On the numerical side, we propose a variational ansatz for the quantum many-body ground state of the fermion system and use the variational Monte Carlo (VMC) approach to identify and simulate the SMG transition. On the theoretical side, we develop a quantum field theory description of the SMG critical point as a fermionic DQCP (fDQCP) and predict its universal properties using renormalization group (RG) analysis. Our numerical results are in good agreement with the analytic predictions, supporting the fractionalization of fermions at the SMG transition.

II. LATTICE MODEL

We investigated a (2+1)D example of SMG. The model is defined on an A-A stacking bilayer honeycomb lattice, as illustrated in Fig. 1(a), with each site i hosting four complex fermion modes, denoted as $c_{il\sigma}$, where $l = 1, 2$ labels the two layers and $\sigma = \uparrow, \downarrow$ labels the two spin components. The model is described by the following Hamiltonian:

$$H = -t \sum_{\langle ij \rangle, l, \sigma} (c_{il\sigma}^\dagger c_{jl\sigma} + \text{H.c.}) + J \sum_i \mathbf{S}_{i1} \cdot \mathbf{S}_{i2}, \quad (1)$$

where $\langle ij \rangle$ stands for the nearest-neighboring pairs of sites i and j on the honeycomb lattice. There is no interlayer fermion hopping. The two layers are only coupled by the antiferromagnetic Heisenberg interaction $J > 0$. $\mathbf{S}_{il} = \frac{1}{2} c_{il\alpha}^\dagger \boldsymbol{\sigma}^{\alpha\beta} c_{il\beta}$ denotes the spin operator at site i layer l , with $\boldsymbol{\sigma} = (\sigma_x, \sigma_y, \sigma_z)$ being the Pauli matrices. The relative interaction strength J/t is the only tuning parameter of this model.

Consider the fermion system at half-filling (with zero chemical potential). When $J/t = 0$, the model describes two decoupled layers of graphene, which produces eight gapless Dirac fermions (two valleys \times two layers \times two spins) at low energy. The gapless *Dirac semimetal* phase is stable against small J/t perturbation, as the local interaction J is irrelevant for (2+1)D Dirac fermions under RG. When $J/t \rightarrow \infty$, the interlayer Heisenberg interaction acts on each honeycomb site independently, which leads to a unique gapped ground state $\otimes_i (c_{i1\uparrow}^\dagger c_{i2\downarrow}^\dagger - c_{i1\downarrow}^\dagger c_{i2\uparrow}^\dagger) |0\rangle$ as the direct product of interlayer spin-singlet states. Such an insulating state will be called an *SMG insulator*, as it does not break any symmetry (either lattice or internal) of the model. Given that any band insulator in this half-filled bilayer honeycomb lattice model would necessarily break some symmetry (see Appendix A for symmetry analysis), the interaction effect is essential in achieving the SMG insulator. Therefore, as J/t is increased, we expect a phase diagram as shown in Fig. 1(b), where an *SMG transition*

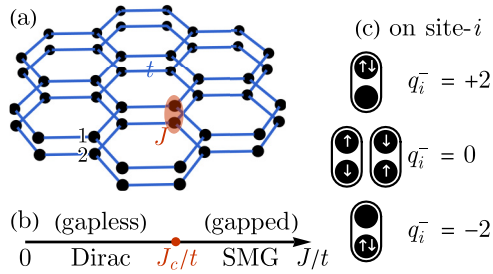


FIG. 1. (a) The bilayer honeycomb lattice model with intralayer hopping t and interlayer Heisenberg coupling J . (b) The phase diagram as J/t varies. (c) On-site fermion configurations of different interlayer $U(1)^-$ charges q_i^- .

happens at some critical J_c (to be determined), separating the Dirac semimetal and the SMG insulator. The model could be relevant to the twisted bilayer graphene [24,25], which has the same Dirac fermion content at low energy, although the interaction may be different. Nevertheless, investigating this toy model is instructive for the future experimental realization of SMG physics in correlated materials.

III. VMC SIMULATION

A. Method

The (2+1)D SMG transition has been numerically observed [7,11] in similar models by quantum Monte Carlo (QMC) simulations. The results suggest that the SMG transition is direct and continuous, but the critical exponent ν (of the correlation length $\xi \sim |J - J_c|^{-\nu}$ scaling) and the fermion operator scaling dimension were not determined yet. To investigate these universal properties of the SMG transition, we proposed a VMC approach [26,27], based on a variational wave function motivated by the parton-Higgs theory [18]. Reference [18] proposes a non-Abelian gauge theory that involves a more complicated confinement mechanism to enter the SMG phase. This work simplifies the field theory, reducing the gauge group to the Abelian group, which allows the direct application of known RG analysis.

Compared to the QMC approach, although the VMC approach is biased by the variational ansatz, it can be pushed to relatively larger system sizes with fewer computational resources. Moreover, the variational wave function provides a unique insight that was not available by other methods, i.e., the mean-field mass. This approach allows us to effectively observe the gap opening of the fermionic parton, which deepens our understanding of the underlying parton physics across the SMG transition.

The construction of the variational state starts with a mean-field (free-fermion) Hamiltonian $H_{\text{MF}}[\lambda] = -t \sum_{\langle ij \rangle, l} (c_{il}^\dagger c_{jl} + \text{H.c.}) + \lambda \sum_i (-)^i (c_{i1}^\dagger c_{i2} + \text{H.c.})$ (with $c_{il} = [c_{i1}, c_{i2}]^T$ including both spins, and spin indices are summed over in H_{MF} implicitly). It introduces an interlayer hopping term λ with a stagger sign $(-)^i = \pm$ between A/B sublattices on the honeycomb lattice. This stagger sign is important to make the λ term to be a mass term that gaps out the Dirac fermions on the mean-field level. λ will be treated as a variational parameter. Consider the ground state

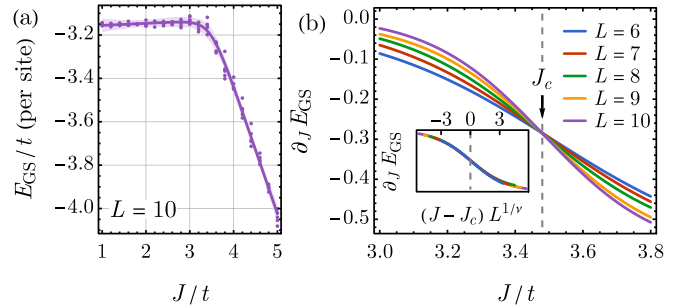


FIG. 2. (a) Ground state energy E_{GS} and (b) its first-order derivative $\partial_J E_{\text{GS}}$ with respect to the interaction strength J . Each dot in (a) represents an estimation of E_{GS} from one VMC simulation.

$|\Psi_{\text{MF}}[\lambda]\rangle$ of $H_{\text{MF}}[\lambda]$ followed by a soft projection (correlation factor) that depends on the configuration of interlayer charge difference $q_i^- := c_{i1}^\dagger c_{i1} - c_{i2}^\dagger c_{i2}$ on every site, as exemplified in Fig. 1(c), the variational many-body state then takes the following form, similar to a Slater-Jastrow wave function [28]

$$|\Psi[\lambda, V]\rangle \propto e^{-V\{q_i^-\}} |\Psi_{\text{MF}}[\lambda]\rangle, \quad (2)$$

where the Jastrow-like energy functional $V\{q_i^-\} = \sum_i V(q_i^-)$ will be variational optimized as well. The objective is to optimize the variational state by minimizing the energy expectation value $\langle \Psi[\lambda, V] | H | \Psi[\lambda, V] \rangle$ given the physical Hamiltonian H in Eq. (1).

The variational state in Eq. (2) is designed to reproduce the exact ground states in both the strong interaction ($J/t \rightarrow \infty$) and the weak interaction ($J/t \rightarrow 0$) limits. In the strong interaction limit, the extreme SMG state corresponds a product of interlayer singlets, which can be obtained by taking the limit of strong interlayer hopping ($\lambda/t \rightarrow \infty$) followed by the hard projection $e^{-V\{q_i^-\}} \propto \prod_i \delta_{q_i^-=0}$ that imposes $q_i^- = 0$ on every site. On the other hand, the exact free-fermion ground state at $J/t = 0$ is achieved by turning off λ and V . This design ensures that the variational state accurately captures the behavior of the system in both limits.

For intermediate J/t , we evaluated the variational energy $\langle \Psi[\lambda, V] | H | \Psi[\lambda, V] \rangle$ by the VMC sampling technique (see Appendix B for algorithm details) and minimized it using the PYTORCH library [29] with the Adam optimizer [30]. This allows us to optimize the variation state by leveraging the autodifferentiation capabilities of PYTORCH. To verify the accuracy of our algorithm, we conducted a benchmark test with exact diagonalization in a single unit cell (consisting of two sites), which shows that our variational ground state can achieve a fidelity of at least 0.99 and has a relative energy excess of at most 10^{-4} across all values of J/t .

B. Numerical results

In our study, we set the energy unit to be $t = 1$ and plotted the ground state energy E_{GS} as a function of the interaction strength J in Fig. 2(a). To estimate E_{GS} at each value of J , we conducted multiple VMC simulations with different initial random seeds and fit a smooth curve to the data. The first-order derivative $\partial_J E_{\text{GS}}$ was then computed based on the fitted energy curve, as shown in Fig. 2(b). The calculations were performed on lattices of $L \times L$ unit cells (totally $2L^2$ sites)

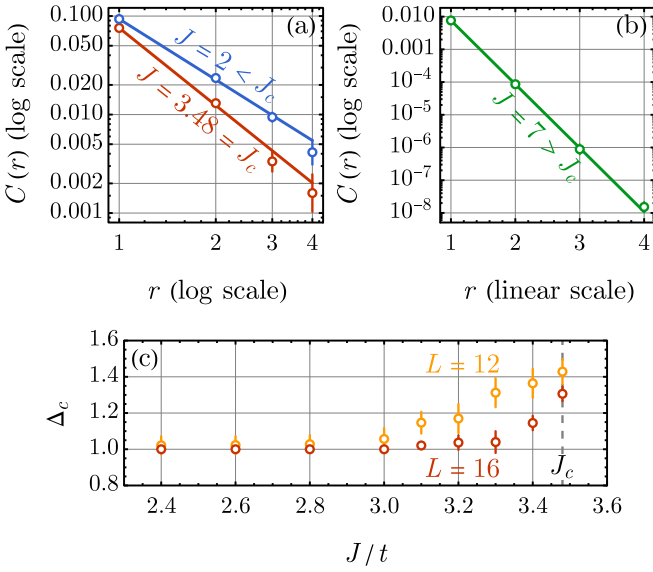


FIG. 3. Fermion-fermion correlation $C(r)$ for (a) $J \leq J_c$ and (b) $J > J_c$, computed on the $L = 16$ lattice. (c) Fermion scaling dimension Δ_c for $J \leq J_c$.

for $L = 6, 7, \dots, 10$. We observed that all curves cross at a single point, which we identified as the SMG critical point $J_c = 3.48$. By rescaling the horizontal axis to $(J - J_c)L^{1/\nu}$, we were able to collapse all curves onto a single curve when the exponent was tuned to $\nu = 0.96 \pm 0.03$, as shown in the inset of Fig. 2(b). This determines the power-law scaling of the correlation length $\xi \sim |J - J_c|^{-\nu}$ near the SMG transition.

To investigate the fermion scaling dimension at the critical point, we measured the fermion-fermion correlation function $C(r) := \langle \Psi[\lambda, V] | c_{i1}^\dagger c_{j1} | \Psi[\lambda, V] \rangle$ between two sites i and j as a function of their separation distance $r = |\mathbf{r}_i - \mathbf{r}_j|$ on a lattice of size $L = 16$. The correlation function $C(r)$ exhibits a power-law behavior $C(r) = 1/r^{2\Delta_c}$ for $J \leq J_c$, as plotted in Fig. 3(a) with the log-log scale. The exponent Δ_c corresponds to the scaling dimension of the fermion operator c_{i1} . We found that the scaling dimension in the Dirac semimetal phase (at $J = 2 < J_c$, for example) is $\Delta_c = 1.00 \pm 0.03$, which is the same as that of the free Dirac fermion in (2+1)D, indicating that the local interaction J is perturbatively irrelevant in this phase. However, at the SMG critical point ($J = J_c$), we observed a distinct scaling dimension of $\Delta_c = 1.31 \pm 0.04$, which suggests a different RG fixed point. In the gapped phase (at $J = 7 > J_c$, for example), we verified that $C(r)$ becomes short-ranged and decays exponentially as expected, as plotted in Fig. 3(b) with the log-linear scale. This clearly signifies that the SMG transition is a semimetal-insulator (gapless to gapped) transition.

The enlarged fermion scaling dimension at the SMG critical point indicates the fractionalization of fermions. To validate this observation more systematically, we extracted the fermion scaling dimension Δ_c by fitting the power-law correlation at different values of $J \leq J_c$ for two system sizes $L = 12, 16$, as shown in Fig. 3(c). As the system size increases (from $L = 12$ to $L = 16$), we observed the trend that Δ_c approaches 1 for $J < J_c$ but seems to converge to some

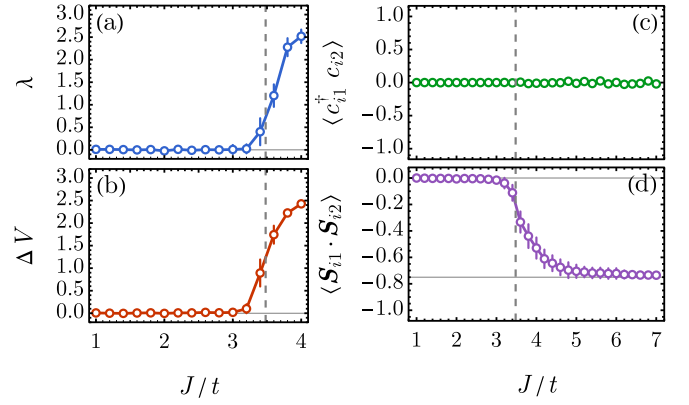


FIG. 4. (a) The interlayer hopping strength λ in the mean-field Hamiltonian $H_{\text{MF}}[\lambda]$. (b) The gap of Jastrow energy $\Delta V = V(\pm 2) - V(0)$ between $q^- = \pm 2$ and $q^- = 0$ configurations, characterizing the strength of the soft projector. (c) The interlayer local fermion coherence (tunneling amplitude). (d) The interlayer local spin-spin correlation. The results are obtained by finite-size scaling to $L \rightarrow \infty$ based on $L = 5, \dots, 10$ VMC simulations (see Appendix C).

finite value above 1 at $J = J_c$. Limited by the available system sizes and the data quality, we were unable to extrapolate our results to infinite system size reliably. Nevertheless, the evidence clearly requires a different conformal field theory (CFT) description of the SMG critical point distinct from the free-fermion CFT.

To better understand the SMG mechanism, we investigated how the variational parameters change across the SMG transition. We found that the staggered interlayer hopping parameter λ in the mean-field Hamiltonian $H_{\text{MF}}[\lambda]$ turns on continuously near the transition, as in Fig. 4(a), resulting in a fermion gap opening in the mean-field state $|\Psi_{\text{MF}}[\lambda]\rangle$. This gap is sufficient to make the fermion-fermion correlation $C(r)$ short-ranged and generate a mass for all fermion excitations in the SMG insulator phase. However, this kind of mass generation comes with the spontaneous breaking of the layer $U(1)^-$ global symmetry that is associated with the conservation of the total interlayer charge difference $Q^- = \sum_i q_i^-$. Under the $U(1)^-$ symmetry, the interlayer hopping term $c_{i1}^\dagger c_{i2}$ transforms as a charge-2 operator. On the mean-field level, a finite λ will induce a finite $\langle c_{i1}^\dagger c_{i2} \rangle$ expectation value on the mean-field state $|\Psi_{\text{MF}}[\lambda]\rangle$, which breaks the $U(1)^-$ symmetry to its \mathbb{Z}_2^- subgroup.

Fortunately, the correlation factor $e^{-V[\{q_i^-\}]}$ helps to restore the $U(1)^-$ symmetry without closing the fermion excitation gap. Recall that the Jastrow-like energy function $V[\{q_i^-\}] = \sum_i V(q_i^-)$ was written as a sum of on-site potentials. We found that the local potential difference $\Delta V = V(\pm 2) - V(0)$ increases across the SMG transition, as shown in Fig. 4(b). The positive ΔV favors the $U(1)^-$ neutral ($q_i^- = 0$) over the $U(1)^-$ charged ($q_i^- = \pm 2$) configurations on every site [see Fig. 1(c) for examples]. As the potential difference ΔV increases, the correlation factor $e^{-V[\{q_i^-\}]}$ suppresses local $U(1)^-$ charge fluctuations, effectively introducing $U(1)^-$ gauge (phase) fluctuations [31–33] due to the quantum mechanical uncertainty relation between the charge and phase observables. As a result, the $\langle c_{i1}^\dagger c_{i2} \rangle$ expectation value is disordered by the gauge

fluctuation, and only those $U(1)^-$ symmetric observables, such as $\langle \mathcal{S}_{i1} \cdot \mathcal{S}_{i2} \rangle$, survive the gauge fluctuation, as clearly shown in Figs. 4(c) and 4(d). This establishes the $J > J_c$ phase as a *symmetric gapped* phase, where the fermion mass (gap) is generated by the condensation of multifermion operators (such as $\mathcal{S}_{i1} \cdot \mathcal{S}_{i2}$) instead of two-fermion operators (such as $c_{i1}^\dagger c_{i2}$).

IV. FIELD THEORY ANALYSIS

The above discussion motivates the fermion fractionalization hypothesis, which states that the physical fermion c_{il} fractionalizes into deconfined bosonic b_{il} and fermionic f_{il} partons at (and only at) the SMG critical point (hence an fDQCP), as

$$c_{il} = \begin{bmatrix} c_{il\uparrow} \\ c_{il\downarrow} \end{bmatrix} = b_{il}^\dagger \begin{bmatrix} f_{il\uparrow} \\ f_{il\downarrow} \end{bmatrix} = b_{il}^\dagger f_{il} \quad (3)$$

for each layer $l = 1, 2$ separately. A parton mean-field analysis can be found in Appendix D. The fermionic parton f_{il} still carries the $SU(2)$ spin quantum number and hops on the honeycomb lattice. However, the separate charge conservation symmetry in each layer l , denoted as $U(1)_l$, is now acting on the bosonic parton b_{il} only. Note that the previously mentioned layer $U(1)^-$ symmetry is a subgroup of the larger $U(1)_1 \times U(1)_2$ symmetry.

The partons b_{il}, f_{il} are redundant descriptions of the physical fermion c_{il} , because the following transformations have no physical effect on Eq. (3):

$$\tilde{U}(1)_l : b_{il} \rightarrow e^{i\theta_n} b_{il}, \quad f_{il} \rightarrow e^{i\theta_n} f_{il}. \quad (4)$$

They are identified as the emergent gauge group $\tilde{U}(1)_1 \times \tilde{U}(1)_2$ arising from the fermion fractionalization. The low-energy physics of the SMG transition in the bilayer honeycomb model can then be described by the following field theory in the parton language:

$$\mathcal{L} = \sum_{l=1,2} |(\partial - i(a_l - A_l))b_l|^2 + r|b_l|^2 + \bar{f}_l \gamma \cdot (\partial - ia_l)f_l, \quad (5)$$

where $l = 1, 2$ labels the two layers. Within each layer l , the theory describes a single-flavor ($N_b = 1$) bosonic scalar field b_l coupled to a four-flavor ($N_f = 4$) fermionic spinor field f_l through the $\tilde{U}(1)_l$ gauge field a_l . The four internal flavors of f_l stand for the spin and valley degrees of freedom inherited from the physical fermion c_l , and γ denotes the γ matrices in the Dirac spinor space. A_l is the background gauge field that track the physical $U(1)_l$ symmetry.

In this field theory Eq. (5), the SMG transition is driven by tuning the only parameter r :

(1) When $r < 0$, the scalar fields b_l condense, pinning the gauge fields a_l to the symmetry background fields A_l through the Higgs mechanism, such that the fermionic partons f_l regain the $U(1)_1 \times U(1)_2$ symmetry charges and restore the gapless physical fermions in the weakly interacting Dirac semimetal phase.

(2) When $r > 0$, the scalar fields b_l are gapped and decoupled from the theory. Driven by the gauge interaction, the fermionic partons can spontaneously develop a parton

TABLE I. State of physical fermion c_l , bosonic b_l and fermionic f_l parton, and gauge fields a_l across SMG transition. $a^\pm = a_1 \pm a_2$ are linear combinations of a_l .

	Dirac semimetal	SMG transition	SMG insulator
c_l	Gapless	Fractionalized	Gapped
b_l	Condensed ($r < 0$)	Critical ($r = 0$)	Gapped ($r > 0$)
f_l	Gapless ($\lambda = 0$)	Gapless ($\lambda = 0$)	Gapped ($\lambda \neq 0$)
a_l	Higgsed	Deconfined	a^- Higgsed a^+ confined

Higgs mass $\lambda(\bar{f}_1 f_2 + \text{H.c.})$, which gaps out all fermions and Higgs the $\tilde{U}(1)_1 \times \tilde{U}(1)_2$ gauge structure down to the diagonal $\tilde{U}(1)^+$ [34]. Then the diagonal $\tilde{U}(1)^+$ gauge field automatically confines at low energy by the Polyakov mechanism [35], leading to a trivially gapped SMG phase. Since A_l does not couple to the parton Higgs field λ , the $U(1)_1 \times U(1)_2$ symmetry remains unbroken even if λ has condensed.

The SMG critical point is therefore described by the field theory Eq. (5) at $r = 0$. The state of various fields across the transition is summarized in Table I.

To estimate the scaling dimension Δ_c of the physical fermion $c_l \sim b_l^\dagger f_l$, we extended the quantum electrodynamics (QED) theory to general N_b bosonic flavors and N_f fermionic flavors and used the result of RG analysis [36,37] by the large- N_b, N_f expansion, which predicted

$$\Delta_c = \frac{3}{2} + \frac{2}{3\pi^2 N_b} - \frac{40}{3\pi^2(N_b + N_f)} + \dots \quad (6)$$

Extrapolating the result to $(N_b, N_f) = (1, 4)$, Eq. (6) predicts $\Delta_c \simeq 1.3 > 1$, which is consistent with our VMC simulation. This provides supportive evidence for the fermion fractionalization hypothesis and establishes the SMG transition as an fDQCP.

V. SUMMARY

We developed a VMC approach to simulate a bilayer honeycomb lattice model and investigated the critical behavior of the SMG transition in this model. We tested the fermion fractionalization hypothesis by measuring the fermion scaling dimension $\Delta_c = 1.31 \pm 0.04$ at the critical point and showing that the result is consistent with the prediction for an fDQCP, $\Delta_c \simeq 1.3 > 1$. The fDQCP field theory indicates that the mean-field parameter λ in the variational state should be interpreted as the Higgs mass of the fermion parton as $\lambda(\bar{f}_1 f_2 + \text{H.c.})$. The VMC simulation explicitly reveals how the parton Higgs mass λ is generated across the SMG transition in Fig. 4(a), providing a deeper understanding of the SMG mechanism from the perspective of the parton Higgs theory [18,38]. Note that the parameter λ is not accessible in other numerical approaches because it is not a gauge-neutral physical observable. This demonstrates the unique advantage of the VMC approach in studying SMG physics. We expect the methodology to apply to more general SMG phenomena in higher dimensions [38–44] or Fermi liquids [45,46], which could have broader implications for the lattice regularization

of chiral fermions [16,47–53], the strong-CP problem [54], and the pseudo-gap phenomenon [55–62].

ACKNOWLEDGMENTS

We acknowledge the helpful discussions with Tarun Grover, Juven Wang, Da-Chuan Lu, and Meng Zeng. We thank Peiyuan Wang for independently checking our calculations in Appendix D. The National Science Foundation supported this research under Grant No. DMR-2238360.

APPENDIX A: SYMMETRY ANALYSIS

The bilayer honeycomb lattice model,

$$H = -t \sum_{(ij),l,\sigma} (c_{il\sigma}^\dagger c_{jl\sigma} + \text{H.c.}) + J \sum_i \mathbf{S}_{i1} \cdot \mathbf{S}_{i2}, \quad (\text{A1})$$

has an $U(1)_1 \times U(1)_2 \times SU(2) \times \mathbb{Z}_2^S$ internal symmetry together with the honeycomb lattice symmetry. Each symmetry and its corresponding transformation to the fermionic operator is listed in Table II, where $c_{il} = [c_{il\uparrow}, c_{il\downarrow}]^T$. The sublattice charge-conjugation symmetry \mathbb{Z}_2^S let the fermion modes on one sublattice pick up a minus sign while keeping the fermion modes on the other sublattice unchanged, then take the complex conjugate of both the fermion mode and the imaginary unit i . Other than the internal symmetries listed above, the system also has honeycomb lattice symmetries such as translation, rotation, reflection, etc. Most importantly, the \mathbb{Z}_2^S and translation symmetry together rule out the possibility of adding any fermionic bilinear terms to gap out the Dirac fermions. Therefore, the gapless Dirac semimetal phase is protected by the symmetries at the free-fermion level.

This statement can be proven more explicitly as follows. When $J = 0$, the free hopping Hamiltonian on honeycomb lattice gives rise to the graphene band structure that produces $2 \times 2 \times 2 = 8$ (two layers, two spins, and two valleys) gapless Dirac fermions $\psi_{Ql\sigma}$ at low energy. They can be described by the low-energy effective field theory Lagrangian

$$\mathcal{L} = \sum_{Ql\sigma} \bar{\psi}_{Ql\sigma} \gamma^\mu \partial_\mu \psi_{Ql\sigma}, \quad (\text{A2})$$

where $Q = K, K'$ labels the two valleys from fermion doubling and $\gamma^\mu = (\sigma^2, \sigma^1, \sigma^3)$, $\bar{\psi}_{Ql\sigma} = \psi_{Ql\sigma}^\dagger \gamma^0$.

Following the existing literature, it is convenient to use the Majorana basis in Hamiltonian formulation, such that eight complex Dirac fermions can be described by an effective

Hamiltonian with matrices of size 32×32 ,

$$H = \int d^2\mathbf{x} \chi^\dagger h_{\times 32} \chi, \quad h_{\times 32} = \sum_{a=1}^2 i\partial_a \alpha^a + \sum_b^5 m_b \beta^b, \quad (\text{A3})$$

where α^a are symmetric matrices, β^b are antisymmetric matrices, and all the α^a, β^b anticommute with each other. Here the $\chi^\dagger m_b \beta^b \chi$ terms represent all the possible bilinear mass terms that can be added to the effective theory. The strategy is to list all possible mass terms and then test whether they are invariant under the required symmetries. The complete Hamiltonian with all possible bilinear mass terms is

$$h_{\times 32} = i\partial_1 \sigma^{30000} + i\partial_2 \sigma^{13000} + m_1 \sigma^{20000} + m_2 \sigma^{11200} + m_3 \sigma^{11200} + m_4 \sigma^{11320} + m_5 \sigma^{12000} \quad (\text{A4})$$

where $\sigma^{ab\dots} = \sigma^a \otimes \sigma^b \otimes \dots$ are the Pauli matrices.

Among the $U(1)_1 \times U(1)_2 \times SU(2) \times \mathbb{Z}_2^S$ symmetries and lattice symmetries we need to concern, it turns out just the translation symmetry plus \mathbb{Z}_2^S can already rule out all the bilinear mass terms. Following the existing literature, the translation symmetry and \mathbb{Z}_2^S can be combined to create an emergent antiunitary symmetry \mathbb{Z}_4^{TF} at low energy: $\psi_{Ql\sigma} \rightarrow i\gamma^0 \psi_{Ql\sigma}^\dagger, i \rightarrow -i$. Translating this symmetry transformation into the Majorana basis becomes

$$\mathbb{Z}_4^{TF} : \psi_{Ql\sigma} = \begin{pmatrix} \psi_{Ql\sigma 1} \\ \psi_{Ql\sigma 2} \end{pmatrix} \rightarrow \begin{pmatrix} -\psi_{Ql\sigma 2}^\dagger \\ \psi_{Ql\sigma 1}^\dagger \end{pmatrix}, \quad i \rightarrow -i$$

$$\chi_{Ql\sigma} = \begin{pmatrix} \chi_{Ql\sigma 11} \\ \chi_{Ql\sigma 12} \\ \chi_{Ql\sigma 21} \\ \chi_{Ql\sigma 22} \end{pmatrix} \rightarrow \begin{pmatrix} -i\chi_{Ql\sigma 21} \\ i\chi_{Ql\sigma 22} \\ i\chi_{Ql\sigma 11} \\ -i\chi_{Ql\sigma 12} \end{pmatrix}, \quad i \rightarrow -i, \quad (\text{A5})$$

and the symmetry transformation in the Majorana basis can be written as $\mathbb{Z}_4^{TF} : \chi_{Ql\sigma} \rightarrow M \cdot \chi_{Ql\sigma}, i \rightarrow -i$, where $M = \sigma^{23000}$. Now we can verify the dynamical part of the Hamiltonian is invariant under $M^\dagger \cdot i\sigma^a \cdot M, i \rightarrow -i, (a = 30\,000, 13\,000)$ but fails after acting on every bilinear mass terms $M^\dagger \cdot \sigma^b \cdot M, i \rightarrow -i, (b = 20\,000, 11\,120, 11\,200, 11\,320, 12\,000)$.

However, the system can still have an on-site Heisenberg interaction while preserving the internal symmetries, results in a symmetric gap state at a strong coupling limit. Therefore, one can expect a SMG transition between both sides. Since there lacks a symmetry-breaking order parameter to distinguish the phases on both sides, such exotic transition is beyond the Landau-Ginzburg-Wilson paradigm and is interesting to study.

APPENDIX B: VARIATIONAL MONTE CARLO ALGORITHM

1. Variational ansatz

The VMC simulation is based on a mean-field ansatz

$$H_{\text{MF}} = -t \sum_{(ij)l\sigma} c_{il\sigma}^\dagger c_{jl\sigma} + \lambda \sum_{i,\sigma} (-)^i c_{i1\sigma}^\dagger c_{i2\sigma} + \text{H.c.} \quad (\text{B1})$$

TABLE II. Internal symmetry of the bilayer honeycomb model.

Internal symmetries		
Conservation	Symmetry group	Transformation
Intralayer charge conservation	$U(1)_1 \times U(1)_2$	$c_{il} \rightarrow e^{-i\theta_l} c_{il}$
Interlayer spin conservation	$SU(2)$	$c_{il} \rightarrow e^{-\frac{i}{2}\theta \cdot \sigma} c_{il}$
Sublattice charge conjugation	\mathbb{Z}_2^S	$c_{il} \rightarrow (-)^i c_{il}$ $i \rightarrow -i$

The mean-field Hamiltonian H_{MF} can be solved exactly. Letting $|\Psi_{\text{MF}}[\lambda]\rangle$ be the ground state of H_{MF} , we assume that the true many-body ground state of the original Hamiltonian Eq. (A1) can be modeled by $|\Psi_{\text{MF}}[\lambda]\rangle$, followed by a soft projection,

$$|\Psi[\lambda, V]\rangle = \mathcal{P}[V]|\Psi_{\text{MF}}[\lambda]\rangle$$

$$\mathcal{P}[V] = \mathcal{P}_{\text{global}} \exp \left[- \sum_i V(q_i) \right], \quad (\text{B2})$$

where $q_i = (q_i^+, q_i^-)$ is the local charge vector specified by on-site state configurations, defined by

$$q_i^\pm := \sum_{l\sigma} (\pm)^l c_{il\sigma}^\dagger c_{il\sigma}. \quad (\text{B3})$$

In general, to model the true ground state, $V(q_i)$ is parametrized by a neural network (a multilayer feed-forward model) and then optimized by deep learning. In our case, since the Hamiltonian is invariant under charge $U(1)^+$ and layer $U(1)^-$ symmetries,

$$Q^\pm := \sum_i q_i^\pm = \sum_{il\sigma} (\pm)^l c_{il\sigma}^\dagger c_{il\sigma},$$

$$[H, Q^\pm] = 0. \quad (\text{B4})$$

The many-body ground state must be in the global charge neutral $Q^\pm = 0$ subspace, so a global projection operator $\mathcal{P}_{\text{global}}$ is introduced to project to the $Q^\pm = 0$ subspace.

2. Sampling through Markov chain

Following the existing literature, the mean-field wave function can be computed by an unitary transformation of H_{MF} . Denoting the diagonal form of the mean-field Hamiltonian as $H_{\text{MF}} = \sum_\mu \epsilon_\mu \gamma_\mu^\dagger \gamma_\mu$ and eigenstates $|\phi_\mu\rangle = \gamma_\mu^\dagger |0\rangle$, the explicit form of the unitary matrix of system with L sites and four flavors ($\sigma = \uparrow, \downarrow, l = 1, 2$) is

$$U = \begin{pmatrix} \langle 1|\phi_1\rangle & \dots & \langle 1|\phi_{4L}\rangle \\ \vdots & \ddots & \vdots \\ \langle 4L|\phi_1\rangle & \dots & \langle 4L|\phi_{4L}\rangle \end{pmatrix}. \quad (\text{B5})$$

The wave-function amplitude can be computed by a Slater determinant,

$$\langle x|\Phi_{\text{MF}}\rangle = \langle x_1, \dots, x_{N_e} | \gamma_1^\dagger, \dots, \gamma_{N_e}^\dagger | 0 \rangle$$

$$= \det \begin{pmatrix} \langle x_1|\phi_1\rangle & \dots & \langle x_1|\phi_{N_e}\rangle \\ \vdots & \ddots & \vdots \\ \langle x_{N_e}|\phi_1\rangle & \dots & \langle x_{N_e}|\phi_{N_e}\rangle \end{pmatrix} = \det \mathbf{D}, \quad (\text{B6})$$

where N_e is the electron number at half filling in our model. Introducing the auxiliary matrix \mathbf{M} , the wave-function ratio

can be obtained as

$$\frac{\langle x'|\Phi_{\text{MF}}\rangle}{\langle x|\Phi_{\text{MF}}\rangle} = \frac{\det \mathbf{D}'}{\det \mathbf{D}} = \sum_m D_{m\beta}^{-1} M_{lm} = W_{l\beta},$$

$$\mathbf{M} = \begin{pmatrix} \langle 1|\phi_1\rangle & \dots & \langle 1|\phi_{N_e}\rangle \\ \vdots & \ddots & \vdots \\ \langle 4L|\phi_1\rangle & \dots & \langle 4L|\phi_{N_e}\rangle \end{pmatrix}, \quad (\text{B7})$$

$$\mathbf{W} = \mathbf{M} \cdot \mathbf{D}^{-1}.$$

where the configuration $|x'\rangle$ is achieved by moving the x_β electron onto site l . The key point that reduces the computational complexity is that the \mathbf{W} matrix can be updated based on what we already have,

$$W'_{h\alpha} = W_{h\alpha} - \frac{W_{h\beta}}{W_{l\beta}} (W_{l\alpha} - \delta_{\alpha\beta}). \quad (\text{B8})$$

Using this update rule, the wave-function amplitude can be computed with the least effort along the sampling. The samples are collected through the Markov chain, such that the algorithm proceeds in the following way:

(1) Starting from a configuration $|x\rangle$, a new configuration is generated by transition probability $T(x'|x)$.

(2) Compute probability ratio $A(x'|x) = \frac{p(x')}{p(x)}$, if $A(x'|x) > 1$, accept new configuration; if $A(x'|x) < 1$, accept new configuration with probability of $A(x'|x)$.

(3) The sampling process is then iterated till equilibrium.

After collecting the configurations along the sampling, the physical quantity $O(x)$ and probability $p(x)$ of each configuration can be computed to obtain expectation values and the objective function. Finally, the parameters of the model (λ in the mean-field ansatz and several other parameters in the potential function V) will be updated by backward propagation through the objective function.

3. Compute expectation value and the objective function

Let $|x\rangle_{x \in X}$ be a complete basis of the many-body Hilbert space (with total electric charge and total valley charge neutral). The expectation value of any observable O can be written as

$$\langle O \rangle = \frac{\langle \Psi | O | \Psi \rangle}{\langle \Psi | \Psi \rangle} = \sum_x O(x) p(x), \quad (\text{B9})$$

with

$$O(x) = \frac{\langle \Psi | O | x \rangle}{\langle \Psi | x \rangle} = \sum_{x'} \frac{\langle \Psi | x' \rangle}{\langle \Psi | x \rangle} \langle x' | O | x \rangle,$$

$$p(x) = \frac{|\langle \Psi | x \rangle|^2}{\sum_x |\langle \Psi | x \rangle|^2}. \quad (\text{B10})$$

To sample from $p(x)$, follow the Markov chain with the transition probability

$$p(x'|x) = \frac{p(x')}{p(x)} = \left| \frac{\langle \Psi | x' \rangle}{\langle \Psi | x \rangle} \right|^2. \quad (\text{B11})$$

The many-body basis $|x\rangle$ is chosen to be the eigenbasis of the projection operator $\mathcal{P}[g]$, such that the amplitude ratio can be

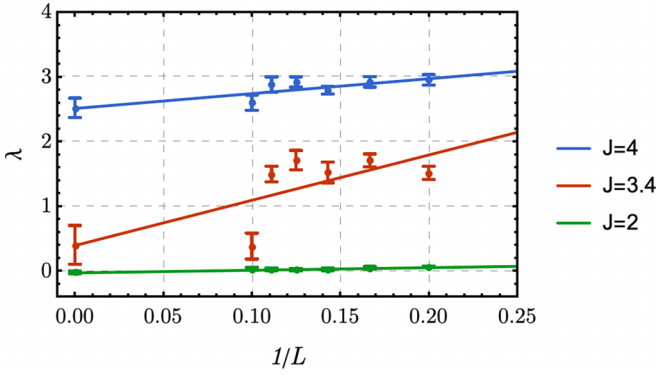


FIG. 5. Extrapolation of Fig. 4(a).

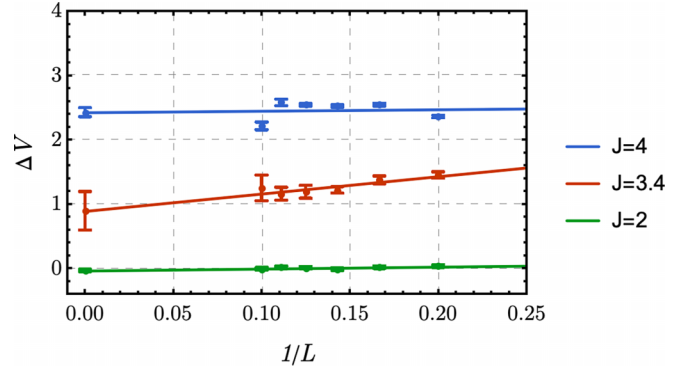


FIG. 6. Extrapolation of Fig. 4(b).

evaluated as

$$\frac{\langle \Psi | x' \rangle}{\langle \Psi | x \rangle} = \frac{\langle \Psi_{\text{MF}}[u] | x' \rangle \langle x' | \mathcal{P}[E] | x' \rangle}{\langle \Psi_{\text{MF}}[u] | x \rangle \langle x | \mathcal{P}[E] | x \rangle}. \quad (\text{B12})$$

The Monte Carlo expectation value of the physical quantity is approximated by

$$\langle O \rangle = \sum_x O(x) p(x) \sim \frac{1}{N} \sum_{x \in \mathcal{S}} O(x), \quad (\text{B13})$$

where $\mathcal{S} \in X$ is a multisubset of all configurations. This approximation lies on the fact that, through Markov chain sampling, the number of visits of a configuration $|x\rangle$ is proportional to its probability $p(x)$. The objective function to minimize is

$$\begin{aligned} \mathcal{L} &= \sum_x [\langle H \rangle - H(x)] \log p_\theta(x) \\ \langle H \rangle &= \sum_x H(x) p(x) \sim \frac{1}{N} \sum_{x \in \mathcal{S}} H(x), \end{aligned} \quad (\text{B14})$$

where θ denotes the set of all parameters of the variational model.

APPENDIX C: FINITE-SIZE SCALING

Here, we provide examples of extrapolating numerical results of finite spacial system size ($L = 5, 6, 7, 8, 9, 10$) to one of infinite size. The results of these extrapolations are used to make Fig. 4. The finite-size extrapolation for subfigures Figs. 4(a), 4(b), 4(d) are separately shown in Figs. 5, 6, 7

APPENDIX D: MEAN-FIELD ANALYSIS

The fermion fractionalization theory can be used to understand the SMG transition. Consider writing a physical fermion mode on each site as a combination of bosonic parton and fermionic parton.

$$c_{il} = \begin{bmatrix} c_{il\uparrow} \\ c_{il\downarrow} \end{bmatrix} = b_{il} \begin{bmatrix} f_{il\uparrow} \\ f_{il\downarrow} \end{bmatrix} = b_{il} f_{il}. \quad (\text{D1})$$

The original Hamiltonian Eq. (A1) can be rewritten as

$$H = -t \sum_{\langle ij \rangle | \sigma} b_{il}^\dagger b_{jl} f_{il\sigma}^\dagger f_{j\sigma} + \text{H.c.} + J \sum_i b_{i1}^\dagger b_{i1} b_{i2}^\dagger b_{i2} S_{i1}^f S_{i2}^f, \quad (\text{D2})$$

where the fermionic parton spin has the form $S_{il}^f = \frac{1}{2} f_{il\alpha}^\dagger \sigma^{\alpha\beta} f_{il\beta}$. The partons are redundant descriptions of the original physical fermion, such that the following transformation has no physical effect:

$$\begin{aligned} b_{il} &\rightarrow e^{-i\theta_n} b_{il} \\ f_{il} &\rightarrow e^{i\theta_n} f_{il}. \end{aligned} \quad (\text{D3})$$

An emergent gauge group $\tilde{U}(1)_1 \times \tilde{U}(1)_2$ arises from the fermion fractionalization; the gift of this redundant description is that one can assign the original $U(1)_l$ layer charge onto the bosonic parton and write down a bilinear term for the fermionic parton without breaking any original symmetry. The charge assignments for physical fermions and bosonic or fermionic partons are specified in Table III.

We present a mean-field analysis of the fractionalized Hamiltonian Eq. (D2). The Hamiltonian can be split into a bosonic parton part and a fermionic parton part under mean-field approximation, such that $H_{\text{MF}} = H_b + H_f$. The Heisenberg interaction $S_{i1} S_{i2}$ can be further simplified as spin-exchange interaction $f_{i2}^\dagger f_{i1} f_{i1}^\dagger f_{i2}$ between layers, which plays the same role as spin-spin interaction with only XY components. The bosonic parton Hilbert space is simplified as the Hilbert space of quantum rotor denoted as $b^\dagger \sim e^{i\theta_n}$.

After some change of variables, as listed in Table IV, the mean-field bosonic Hamiltonian becomes on-site and the mean-field fermionic Hamiltonian is quadratic, such that each

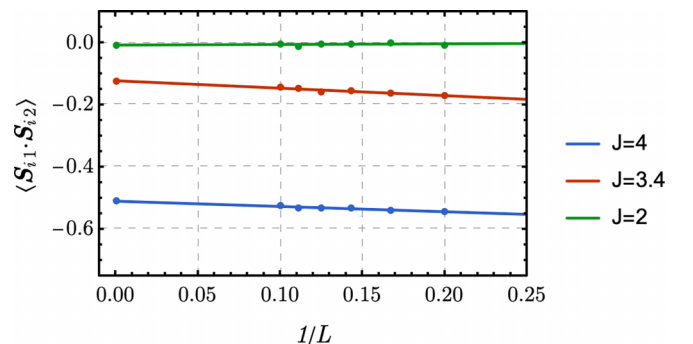


FIG. 7. Extrapolation of Fig. 4(d).

TABLE III. Charge assignment of physical fermion and bosonic fermionic parton. m_i and M_i are the bilinear mass of the physical fermion and fermionic parton, respectively.

	$\tilde{U}(1)_1$	$\tilde{U}(1)_2$	$U(1)_1$	$U(1)_2$	$SU(2)$
c_{i1}	0	0	1	0	2
c_{i2}	0	0	0	1	2
m_i	0	0	1	-1	1
b_{i1}	-1	0	1	0	1
b_{i2}	0	-1	0	1	1
f_{i1}	1	0	0	0	2
f_{i2}	0	1	0	0	2
M_i	1	-1	0	0	1

can be solved self-consistently,

$$\begin{aligned}
 H_b &= \sum_i -6t\phi u e^{i\theta_{i1}} + \text{H.c.} + 12t|\phi|^2 u \\
 &\quad - J e^{-i\theta_{i1}} e^{i\theta_{i1}} e^{-i\theta_{i2}} e^{i\theta_{i2}} |M|^2, \\
 H_f &= -t \sum_{\langle ij \rangle l \sigma} |\phi|^2 J_{il\sigma}^\dagger f_{j l \sigma} + \text{H.c.} \\
 &\quad + \frac{J}{2} \psi \sum_i (|M|^2 - (-)^i M f_{i1}^\dagger f_{i2} - (-)^i M^* f_{i2}^\dagger f_{i1}),
 \end{aligned} \tag{D4}$$

where $|\phi|^2$ and $|M|^2$ play the role of order parameters in the bosonic parton and fermionic parton, respectively, and the factor of 6 = 3 × 2 in H_b is from the number of bonds on the honeycomb lattice for each site. The ground-state energy per site for each part is

$$\begin{aligned}
 E_b &= \frac{1}{2} (-J|M|^2 - 24tu|\phi|^2 - \sqrt{J^2|M|^4 + 576t^2u^2|\phi|^2}), \\
 E_f &= \frac{1}{N} \sum_k^{BZ} J\psi|M|^2 - \sqrt{J^2\psi^2|M|^2 + 4t^2|\phi|^4|f(\mathbf{k})|^2}.
 \end{aligned} \tag{D5}$$

In each part, $|\phi|^2$ and $|M|^2$ are computed by minimizing E_b and E_f , respectively, then the expectation values can be computed self-consistently as $u = \frac{1}{N} \sum_k^{BZ} \frac{t|\phi|^2|f(\mathbf{k})|^2}{3\sqrt{J^2\psi^2|M|^2 + 4t^2|\phi|^4|f(\mathbf{k})|^2}}$ and $\psi = \frac{1}{2} (1 + \frac{J|M|^2}{\sqrt{J^2|M|^4 + 576t^2u^2|\phi|^2}})$.

The ground-state optimization is implemented by:

- (1) Input u and $|M|^2$ to E_b , then minimize $E_b|_{(u, |M|^2)}$ to get $|\phi|^2$, ψ .
- (2) Input $|\phi|^2$ and ψ to E_f , then minimize $E_f|_{(|\phi|^2, \psi)}$ to get $|M|^2$, u .
- (3) Iterate till equilibrium.

TABLE IV. Mean-field change of variables.

$\langle e^{i\theta_{i1}} \rangle$	ϕ
$\langle e^{-i\theta_{i1}} e^{i\theta_{i1}} e^{-i\theta_{i2}} e^{i\theta_{i2}} \rangle$	ψ
$\langle J_{i1\sigma}^\dagger f_{j l \sigma} \rangle$	u
$\langle J_{i2}^\dagger f_{i1} \rangle$	$(-)^i 2M$

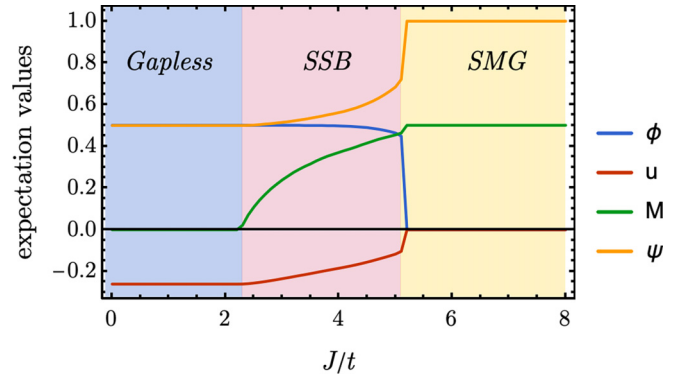


FIG. 8. Mean-field result and phase diagram.

The result is shown in Fig. 8.

(1) In the weak coupling limit, the fermion site-hopping expectation value recovers the result of the Dirac semimetal $u \sim -0.26$, the interlayer hopping amplitude $|M|^2$ is 0, and the bosonic parton is at superfluid state $|\phi|^2 > 0$. This corresponds to the gapless Dirac semimetal phase.

(2) In the strong coupling limit, the fermionic parton opens up interlayer hopping order $|M|^2 > 0$, and the bosonic parton is at gap state $|\phi|^2 = 0$. Although the fermionic parton bilinear mass is condensed,

$$H_M = \sum_i M_i f_{i1}^\dagger f_{i2} + \text{H.c.}, \tag{D6}$$

it does not break any symmetry, but only to Higgs down the gauge group. The resulting state is symmetric and gapped (for both bosonic and fermionic partons), which corresponds to the SMG insulator phase.

(3) However, the mean-field theory also predicts an intermediate phase, where $|M|^2 > 0$ and $|\phi|^2 > 0$, then $\phi M = m$ will combine into the physical fermion bilinear mass term m , which breaks the physical $U(1)_1 \times U(1)_2$ symmetry. This corresponds to a spontaneous symmetry breaking (SSB) phase, where the system develops interlayer exciton order. Nevertheless, as we have shown in the main text, the more reliable VMC simulation rules out such an intermediate phase.

In the mean-field theory, the gapless-SSB transition is continuous, see Fig. 9, while the SSB-SMG transition is of the first order (which is obvious from the jump of mean-field parameters).

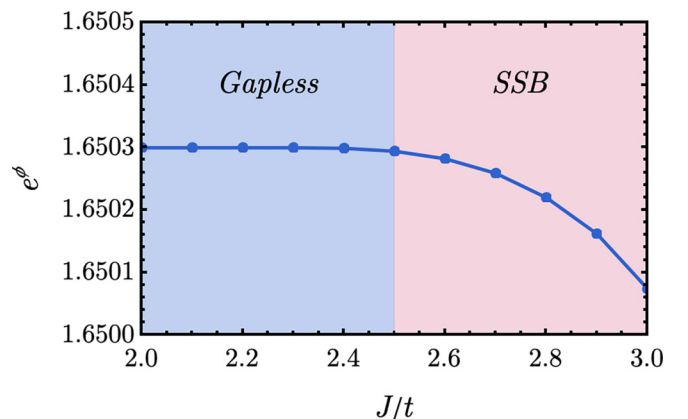


FIG. 9. Zoom-in version of the bosonic order parameter.

- [1] J. Wang and Y.-Z. You, *Symmetry* **14**, 1475 (2022).
- [2] P. W. Anderson, *Phys. Rev.* **130**, 439 (1963).
- [3] F. Englert and R. Brout, *Phys. Rev. Lett.* **13**, 321 (1964).
- [4] P. W. Higgs, *Phys. Rev. Lett.* **13**, 508 (1964).
- [5] G. S. Guralnik, C. R. Hagen, and T. W. B. Kibble, *Phys. Rev. Lett.* **13**, 585 (1964).
- [6] S. Weinberg, *Phys. Rev. Lett.* **19**, 1264 (1967).
- [7] K. Slagle, Y.-Z. You, and C. Xu, *Phys. Rev. B* **91**, 115121 (2015).
- [8] V. Ayyar and S. Chandrasekharan, *Phys. Rev. D* **91**, 065035 (2015).
- [9] S. Catterall, *J. High Energy Phys.* **01** (2016) 121.
- [10] V. Ayyar and S. Chandrasekharan, *Phys. Rev. D* **93**, 081701(R) (2016).
- [11] Y.-Y. He, H.-Q. Wu, Y.-Z. You, C. Xu, Z. Y. Meng, and Z.-Y. Lu, *Phys. Rev. B* **94**, 241111(R) (2016).
- [12] V. Ayyar and S. Chandrasekharan, *Phys. Rev. D* **96**, 114506 (2017).
- [13] N. Butt, S. Catterall, and D. Schaich, *Phys. Rev. D* **98**, 114514 (2018).
- [14] S. Catterall, N. Butt, and D. Schaich, [arXiv:2002.00034](https://arxiv.org/abs/2002.00034).
- [15] N. Butt, S. Catterall, and G. C. Toga, [arXiv:2111.01001](https://arxiv.org/abs/2111.01001).
- [16] M. Zeng, Z. Zhu, J. Wang, and Y.-Z. You, *Phys. Rev. Lett.* **128**, 185301 (2022).
- [17] A. Hasenfratz, *Phys. Rev. D* **106**, 014513 (2022).
- [18] Y.-Z. You, Y.-C. He, C. Xu, and A. Vishwanath, *Phys. Rev. X* **8**, 011026 (2018).
- [19] Y.-Z. You, Y.-C. He, A. Vishwanath, and C. Xu, *Phys. Rev. B* **97**, 125112 (2018).
- [20] T. Senthil, A. Vishwanath, L. Balents, S. Sachdev, and M. P. A. Fisher, *Science* **303**, 1490 (2004).
- [21] O. I. Motrunich and A. Vishwanath, *Phys. Rev. B* **70**, 075104 (2004).
- [22] T. Senthil, L. Balents, S. Sachdev, A. Vishwanath, and M. P. A. Fisher, *Phys. Rev. B* **70**, 144407 (2004).
- [23] T. Senthil and M. P. A. Fisher, *Phys. Rev. B* **74**, 064405 (2006).
- [24] Y. Cao, V. Fatemi, A. Demir, S. Fang, S. L. Tomarken, J. Y. Luo, J. D. Sanchez-Yamagishi, K. Watanabe, T. Taniguchi, E. Kaxiras, R. C. Ashoori, and P. Jarillo-Herrero, *Nature (London)* **556**, 80 (2018).
- [25] Y. Cao, V. Fatemi, S. Fang, K. Watanabe, T. Taniguchi, E. Kaxiras, and P. Jarillo-Herrero, *Nature (London)* **556**, 43 (2018).
- [26] D. Ceperley, G. V. Chester, and M. H. Kalos, *Phys. Rev. B* **16**, 3081 (1977).
- [27] S. Sorella, *Phys. Rev. B* **64**, 024512 (2001).
- [28] R. Jastrow, *Phys. Rev.* **98**, 1479 (1955).
- [29] A. Paszke, S. Gross, F. Massa, A. Lerer, J. Bradbury, G. Chanan, T. Killeen, Z. Lin, N. Gimelshein, L. Antiga, A. Desmaison, A. Kopf, E. Yang, Z. DeVito, M. Raison, A. Tejani, S. Chilamkurthy, B. Steiner, L. Fang, J. Bai *et al.*, in *Advances in Neural Information Processing Systems 32* (Curran Associates, Red Hook, 2019), pp. 8024–8035.
- [30] D. P. Kingma and J. Ba, [arXiv:1412.6980](https://arxiv.org/abs/1412.6980).
- [31] O. I. Motrunich, *Phys. Rev. B* **72**, 045105 (2005).
- [32] M. Hermele, Y. Ran, P. A. Lee, and X.-G. Wen, *Phys. Rev. B* **77**, 224413 (2008).
- [33] Z.-Y. Weng, *New J. Phys.* **13**, 103039 (2011).
- [34] The \mathbb{Z}_2 subgroup of $\tilde{U}(1)^-$ is shared with $\tilde{U}(1)^+$, so the Higgsing does not lead to \mathbb{Z}_2 topological order as well.
- [35] A. Polyakov, *Nucl. Phys. B* **120**, 429 (1977).
- [36] R. K. Kaul and S. Sachdev, *Phys. Rev. B* **77**, 155105 (2008).
- [37] S. Benvenuti and H. Khachatryan, *J. High Energy Phys.* **05** (2019) 214.
- [38] D. Tong, *J. High Energy Phys.* **07** (2022) 001.
- [39] S. Catterall and D. Schaich, *Phys. Rev. D* **96**, 034506 (2017).
- [40] V. Ayyar and S. Chandrasekharan, *J. High Energy Phys.* **10** (2016) 058.
- [41] V. Ayyar, [arXiv:1611.00280](https://arxiv.org/abs/1611.00280).
- [42] D. Schaich and S. Catterall, *European Physical Journal Web of Conferences*, European Physical Journal Web of Conferences, Vol. 175 (2018), p. 03004.
- [43] S. Catterall and N. Butt, *Phys. Rev. D* **97**, 094502 (2018).
- [44] S. Catterall, *Phys. Rev. D* **107**, 014501 (2023).
- [45] D.-C. Lu, M. Zeng, J. Wang, and Y.-Z. You, *Phys. Rev. B* **107**, 195133 (2023).
- [46] H. Zhai, F. Wang, and D.-H. Lee, *Phys. Rev. B* **80**, 064517 (2009).
- [47] J. Wang and X.-G. Wen, *Phys. Rev. B* **107**, 014311 (2023).
- [48] M. DeMarco and X.-G. Wen, [arXiv:1706.04648](https://arxiv.org/abs/1706.04648).
- [49] J. Wang and X.-G. Wen, *Phys. Rev. Res.* **2**, 023356 (2020).
- [50] J. Wang and X.-G. Wen, *Phys. Rev. D* **99**, 111501(R) (2019).
- [51] Y. Kikukawa, *Prog. Theor. Exp. Phys.* **2019**, 073B02 (2019).
- [52] S. S. Razamat and D. Tong, *Phys. Rev. X* **11**, 011063 (2021).
- [53] N. Butt, S. Catterall, A. Pradhan, and G. C. Toga, *Phys. Rev. D* **104**, 094504 (2021).
- [54] J. Wang, *Phys. Rev. D* **106**, 125007 (2022).
- [55] M. Franz and A. J. Millis, *Phys. Rev. B* **58**, 14572 (1998).
- [56] H.-J. Kwon and A. T. Dorsey, *Phys. Rev. B* **59**, 6438 (1999).
- [57] H.-J. Kwon, A. T. Dorsey, and P. J. Hirschfeld, *Phys. Rev. Lett.* **86**, 3875 (2001).
- [58] M. Franz and Z. Tešanović, *Phys. Rev. Lett.* **87**, 257003 (2001).
- [59] P. Curty and H. Beck, *Phys. Rev. Lett.* **91**, 257002 (2003).
- [60] Y.-H. Zhang and S. Sachdev, *Phys. Rev. Res.* **2**, 023172 (2020).
- [61] Y.-H. Zhang and S. Sachdev, *Phys. Rev. B* **102**, 155124 (2020).
- [62] X. Wang and Y. Qi, *Phys. Rev. B* **107**, 224502 (2023).